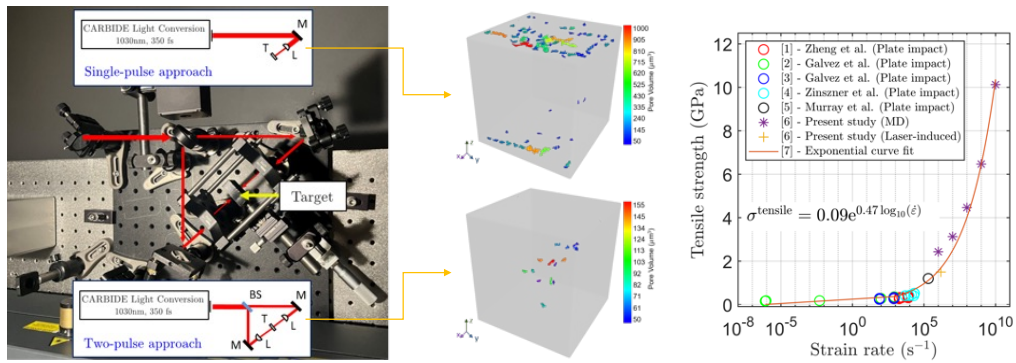


Graphical Abstract

Spall failure of alumina at high-strain rates using femtosecond laser experiments and high-fidelity molecular dynamics simulations

Mewael Isiet, Musanna Galib, Yunhuan Xiao, Jerry I. Dadap, Ziliang Ye, Mauricio Ponga



Spall failure of alumina at high-strain rates using femtosecond laser experiments and high-fidelity molecular dynamics simulations

Mewael Isiet^a, Musanna Galib^a, Yunhuan Xiao^{b,c}, Jerry I. Dadap^{b,c}, Ziliang Ye^{b,c}, Mauricio Ponga^a

^a*Department of Mechanical Engineering, The University of British Columbia, Vancouver, British Columbia, V6T 1Z4, Canada*

^b*Department of Physics & Astronomy, The University of British Columbia, Vancouver, British Columbia, V6T 1Z1, Canada*

^c*Quantum Matter Institute, The University of British Columbia, Vancouver, British Columbia, V6T 1Z1, Canada*

Abstract

Ceramic materials are widely used in high-strain-rate applications due to their exceptional strength-to-weight ratio. However, under these extreme conditions, spall failure becomes a critical concern, which is driven by a large hydrostatic tensile stress state. This study introduces a novel two-laser setup to generate controlled hydrostatic stress states at specific locations within test specimens. By inducing and manipulating shock wave interactions, we achieve large hydrostatic compressive and tensile stresses at very high-strain-rates, enabling the controlled nucleation and growth of nanovoids leading to spall failure. Our experiments demonstrate that shock wave interference can precisely trigger spallation at arbitrary locations in the specimen thickness. To further validate our approach, we investigate alumina spall failure using molecular dynamics (MD) simulations with a custom-designed graph neural network potential. The MD results show strong agreement with experimentally estimated spall strength. These findings highlight the potential of the two-laser technique as a powerful tool for studying the early stages of spall failure in ceramics, paving the way for advanced materials testing methodologies.

Keywords: Laser-induced spall failure, Dynamic failure, High-fidelity molecular dynamics, Alumina, Ceramics, two-laser experiment

1. Introduction

Ceramics have been extensively used in ballistic applications [1, 2, 3, 4] mainly due to their attractive strength to density ratio in comparison to metals [5, 6]. The most commonly used ceramics are alumina (Al_2O_3), silicon carbide (SiC), and boron carbide (B_4C). Amongst these ceramics, alumina due to its low cost and ability to be manufactured using a variety of methods, such as slip casting, powder compacting, injection molding, and additive techniques, has been the preferred material to be used in ballistic protection [7, 8]. These advanced ceramics play an important role within an armor system against projectile impact by effectively dissipating ballistic energy. Unlike metallic armor, which tends to absorb impact energy through plastic deformation via dislocation emission from nanovoids, ceramics tend to fracture to dissipate the kinetic energy of incoming projectiles [5]. Ceramics plates used in armor panels can typically experience high-velocity impacts ranging between 250 to 2000 $\text{m} \cdot \text{s}^{-1}$ [9, 10, 11], generating shock wave propagation at very high-strain-rates. Upon impact, failure takes place leading to the perforation of the ceramic target. These failures occur due to a combination of various mechanisms such as changes in the microstructural features, material strength, impact velocity and orientation, and projectile shape [12]. Ceramics, due to their brittle behavior, fail as a result of either plugging, spall failure, or radial fracture [13, 14]. Due to ceramics' lower tensile strength, compared to their compressive strength, failure due to tensile loading typically occurs first, i.e., spall failure [11, 15].

Spall behavior of alumina has been extensively studied using the plate impact method [16, 17, 18, 19, 20, 21]. Here, the impact of an accelerated flyer plate against a target is used to generate a large hydrostatic tensile state to initiate failure. The overall consensus on the behavior of alumina from plate impact experiments is as follows: (i) spall resistance increases with increase in Al_2O_3 content as impurities introduce flaws which could act as weak spots for the nucleation of voids, (ii) spall behavior is sensitive to pulse duration and initial microstructure, (iii) spall strength tends to decrease with increasing shock pressure due to incremental cracking of the material during the compression phase, and (iv) three failure modes have been observed under microscopy, i.e. fracture nucleation from voids, trans-granular micro-cracks, and inter-granular fracture. Some degree of plastic activity (twinning and deformation bands) have also been identified [16, 22]. These results show the effectiveness of the conventional plate impact method; however, its destruc-

tive, time-intensive nature, need for large samples, and limited strain rates below 10^6 s^{-1} make it unsuitable for high-throughput experiments and studying alumina’s spall behavior at extremely high-strain-rates [23]. Laser-driven shock methods, including the laser-induced impact test [24, 25], laser-driven micro-flyer [26, 27], and two-pulse laser shock [28], have emerged as viable alternatives to conventional techniques. These methods not only achieve strain rates exceeding 10^6 s^{-1} , but also offer advantages such as lower energy requirements for deforming smaller specimens and simplified procedures for aligning diagnostics.

However, since experimental spall studies are confined to free surface diagnostics and *post-mortem* observation [29, 30], it is necessary to incorporate computational methods to understand the failure mechanisms occurring at very small temporal (**fs–ns**) and spatial (**nm**) scales. As a result, molecular dynamics (MD) has served as a competent tool to study the spall behavior of metals (such as Ni [31, 32], Al [33, 34], and Cu [35, 36]), alloys (such as high-entropy alloys [37, 38], magnesium-based alloys [39, 40], and Ni-based alloys [27, 41]), and ceramics, such as Al_2O_3 [42, 43] and SiC [44, 45]. Amongst the spall studies on ceramics, the Vashishtha [46], COMB3 [47], and ReaxFF [48] potentials have been used to model material behavior, and are reactive, charge-and bond-order based. While, generally speaking, these potentials allow the simulation of large and complex phenomena, their accuracy has been questioned for certain applications [49, 50] and as it is not straightforward to modify or extend such potentials readily [51], alternative approaches have been developed to remedy this. Allegro [52, 53], an equivariant graph neural network (GNN) based machine learning model, aims to approximate the potential energy surface using density functional theory (DFT) data to allow for the simulation of large-scale systems.

In this work, we focus on the application of the single- and two-pulse laser shock setup to study the spall behavior of commercially available alumina samples. Typically in spall experiments, time-resolved diagnostics are performed using velocimetry to measure the free-surface velocity, and infer the spall strength [17, 15, 19]. However, in this work, the spall strength is estimated using the spall thickness captured via X-ray micro-computed tomography imaging. Post-mortem analysis of shocked-alumina will be performed to understand the micro-structural failure mechanisms of ceramics. *In-situ* observation will be performed on molecular dynamics using a DFT-based machine learning potential to enable characterization of spallation in alumina ceramics.

2. Methodology

2.1. Laser shock experimental setup

The experimental setup can be seen in Figure 1a where the laser beam is directed to a single surface of the sample in the single-pulse approach or using a series of mirrors and a beam-splitter is used to illuminate the front and back surface of the sample in the two-pulse approach. The ultra-short laser pulses at a maximum energy of $90 \mu\text{J}$ are generated by a femtosecond solid-state laser system (Carbide CB3-40W, Light Conversion) with a pulse duration of 350 fs. Using the laser's internal shutter, a single laser pulse can be emitted with a full width at half maximum of 3.9 mm, and incorporating focusing lenses ensures that the spot size and the laser fluence can be controlled by careful positioning of the sample. More details of the experimental setup can be found in our previous work [28].

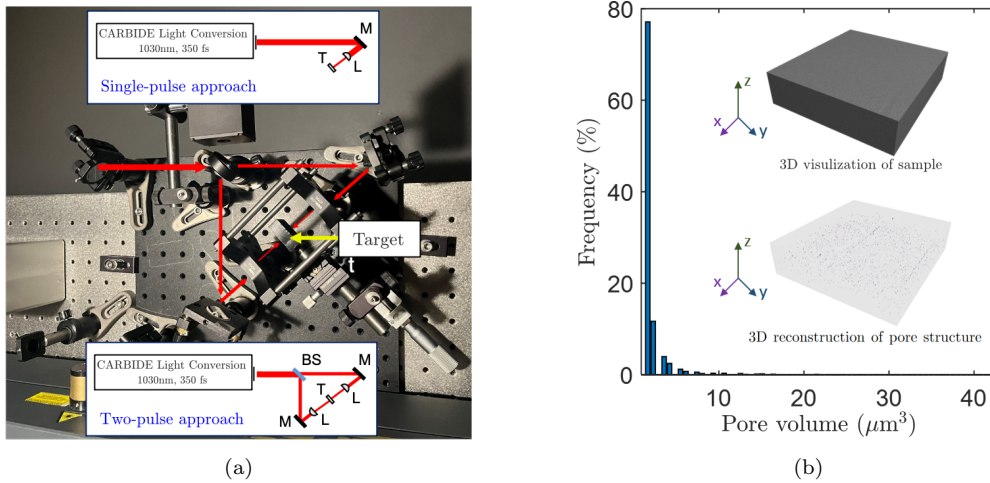


Figure 1: Schematic of the (a) single- and two-pulse laser-induced spallation setups that illuminates either the front surface only or both the front and back surfaces and (b) the histogram of the pore volume of the pristine Al_2O_3 sample with inset images of the micro-CT scan of the solid volume and pore structure.

Commercially available Al_2O_3 (Lithoz America) samples with 99.8% purity and a thickness of $250 \mu\text{m}$ were used in this study. The porosity of the printed Al_2O_3 was analyzed using an X-ray micro-computed tomography scan (micro-CT, Zeiss Xradia 520 Versa) with a voxel resolution of $1 \mu\text{m}$. A 3D reconstruction of the sample revealed small voids, resulting in a porosity

of less than 0.01% with a mean pore volume of $1.95 \mu\text{m}^3$, with the smallest, largest, and 95th percentile pore volumes measuring $1 \mu\text{m}^3$, $42 \mu\text{m}^3$, and $3.58 \mu\text{m}^3$, as shown in Figure 1b . The porosity analysis was carried out using the Dragonfly software [54] by following the common procedure outlined in the literature [55, 56]. Due to the transparency of Al_2O_3 to laser radiation, a thin coating of Ni ($\sim 100 \text{ nm}$) was deposited on the front and back surfaces through physical vapor deposition. When irradiated, the laser beams induce a rapid energy absorption and temperature increase in the Ni coating, which in turn generates a compressive shock wave followed by a release wave that propagates into the Al_2O_3 substrate. The interaction of these release waves creates a high hydrostatic tensile state, leading to spall failure if the stress exceeds the spall strength of Al_2O_3 . Here, the spall strength will be determined experimentally through the spall thickness method [57, 58, 28] and compared to high-fidelity interatomic potential under molecular dynamics.

2.2. Computational setup

Density Functional Theory (DFT) Simulations

Kohn-Sham density-functional theory (KS-DFT) [59, 60] was employed through plane-wave-based implementation within the Vienna Ab-Initio Simulation Package (VASP) [61]. The generalized gradient approximation (GGA) of Perdew, Burke, and Ernzerhof (PBE) [62] was employed as the semilocal exchange-correlation functionals, and the projector augmented-wave (PAW) [63] pseudopotentials were used to express the atom core electrons. The total energy was minimized for the alumina supercell (16 unit cells) in all possible degrees of freedom (ionic positions, alumina cell shape, and volume) to determine the optimal relaxed geometry using the self-consistent method where partial wave occupancies were calculated by Gaussian smearing width of 0.026 eV as shown in previous study [64]. The electronic energies cut-off and the kinetic-energy cutoff E_{cut} are set to 10^{-6} eV and $1 \text{ meV}\cdot\text{atom}^{-1}$, respectively. A $4 \times 4 \times 4$ Monkhorst-Pack k -points are used as mesh for the alumina crystal to produce the plane wave basis set. After fully relaxing the structure, the alumina cell is strained hydrostatically in all directions up to $\pm 20\%$ of the lattice parameter with a stepsize of 0.01% (4000 instances) using AtomProNet python package [65], and self-consistent field (SCF) calculations are performed to get the geometric features required for Euclidian neural network training. To include the effect of porosity in the potential energy surface from machine learning potential, four different structures were optimized and hydrostatically strained in DFT simulations, namely- pure

alumina, alumina with O vacancy, alumina with Al vacancy, and alumina with both Al, O vacancies.

Equivariant neural network interatomic potential

Equivariant graph neural networks (GNN) based on a 3D Euclidean group have been used to perform symmetry operations [66]. In a graph-based representation of alumina atomic structure, Al and O atoms can be present as the nodes (n_i, n_j) respectively, and bonds are the edges (e_{ij}). Here, we used Allegro [53], an equivariant neural network for a local atomic environment, where scalar and vector features of each atom pass using two-body multi-layer perception (ϕ). The alumina GNN model was trained with a total allocation of 16000 structures generated through self-consistent DFT calculation, divided into 14000 for training and 2000 for validation.

All rotations, translations, and reflections symmetry have been preserved in the orthogonal Euclidean group $\mathcal{O}(3)$ symmetry operations. We used one Allegro layer with one feature of even parity and the hyperparameter that controls maximum rotation, $l_{max}=1$. The two-body latent multi-layer perceptron (MLP) comprised of three hidden layers of dimensions [32, 64, 128] using SiLU nonlinearities [67] and uniform initialization. The subsequent latent MLP consisted of a single hidden layer with dimension 128, also using a SiLU nonlinearity and uniform initialization, with latent ResNet enabled. The final edge energy MLP had a hidden layer of dimension 32 with uniform initialization and no nonlinearity. Another self-interaction layer reduced the feature dimension to a single scalar output value per atom. The total potential energy was obtained by summing these scalar outputs over all atoms. Forces were derived as the negative gradient of the predicted total potential energy, calculated via automatic differentiation. We used a radial cutoff of 3.0 Å. The GNN model was trained using a combined loss function of energies and forces. The loss function weights forces and total energy equally, and the training was performed using the Adam optimizer [68] in PyTorch [69]. The learning rate and the batch size for this GNN training were 0.002 and 1, respectively. Based on the validation loss, an on-plateau scheduler was employed to decrease the learning rate. The patience was set to 50, and the decay factor was set to 0.5. We employed an exponential moving average, with a weight of 0.99, to assess both the validation set and the final trained model. Early stopping criteria include a lower bound learning rate of 10^{-5} and patience of 100 epochs for validation loss. The dataset was randomly rearranged after each epoch and trained using the float32 data type. The

GNN model was trained on a single NVIDIA V100 GPU.

Nanovoid molecular dynamic simulations

The pre-trained Allegro potential energy surface was used in LAMMPS [70] to perform classical molecular dynamics simulations. Unless otherwise stated, the simulation cell dimensions were set to $62a_o \times 60b_o \times 42c_o$ corresponding to a total of 30^3 unit cells (containing 3,248,624 atoms), where $a_o = 4.85 \text{ \AA}$, $b_o = 4.99 \text{ \AA}$, and $c_o = 7.09 \text{ \AA}$ are the lattice parameters of the Al_2O_3 unit cell [71, 72, 73]. An initial void of d_v was created at the center by removing atoms from the bulk Al_2O_3 super-cell. Here, as well unless stated, $d_v = 6 \text{ nm}$ resulting in a void volume fraction ($V_{\text{void}}/V_{\text{cell}}$) of 0.4%. Finally, periodic boundary conditions were applied to the simulation cell to simulate an infinitely large system. Before loading, the total energy of the Al_2O_3 super-cell was minimized by iteratively adjusting atom coordinates. Once minimized, the structure was equilibrated at $T = 300 \text{ K}$ and zero pressure by employing an isothermal-isobaric ensemble for a total duration of 100 ps [74].

The relaxed structure was then subjected to a controlled deformation gradient, $\mathbf{F} = (1 + \dot{\epsilon}\Delta t)\mathbf{I}$, to simulate hydrostatic loading, where \mathbf{I} is a 3×3 identity matrix, $\dot{\epsilon}$ is the applied strain rate, and $\Delta t = 5 \text{ fs}$ is the time-step. Virial stress was computed using the conventional method [75] from which the hydrostatic stress $\sigma = (\sigma_1 + \sigma_2 + \sigma_3)/3$ was calculated using the principal stress σ_i . Volumetric and deviatoric strains were calculated from the atomic Green-Lagrange strain tensor for each atom and averaged with respect to a pre-defined volume to establish a continuum strain measure. Lastly, OVITO was used to visualize the atomic trajectory and analyze spall failure [76].

3. Results

3.1. Laser spall experiments of alumina

Next, we examine the surface response of the nickel coated Al_2O_3 samples under the single- and two-pulse laser spall approach. The stress-strain curves shown in Figure 5b indicate the amount of hydrostatic tensile stress required to drive spall failure, as a function of the strain rate. Using the analytical solution of the two-temperature model [28], we can relate the laser fluence to the maximum tensile stress developed in the thin Ni coating, as demonstrated in Figure 2a. As seen in the figure, for a fixed spot size of $\sim 250 \mu\text{m}$, both the laser fluence and the resulting tensile stress can be controlled by adjusting the pulse energy. The incident stress waves (σ_1), generated in the

Ni coating, propagate towards the Al_2O_3 substrate. Upon reaching the Ni- Al_2O_3 interface, a portion of the stress wave (80%) is transmitted (σ_T) to the center of the sample, while a smaller fraction (20%) is reflected (σ_R) back to the free surface. The ratio of transmitted to reflected stress is governed by the shock impedance of the materials. The density (ρ) of Al_2O_3 and Ni are 3,890 and 8,900 $\text{kg}\cdot\text{m}^{-3}$, respectively; bulk sound speed (C) of Al_2O_3 and Ni are 7,455 and 4,850 $\text{m}\cdot\text{s}^{-1}$, respectively [17, 77]. Prior to reaching the interface, following laser-matter interaction, the Ni coating experiences a rapid increase in temperature and pressure, and propagates shockwaves towards the Al_2O_3 substrate, containing a compression front followed by an unloading tensile wave, as shown in Figure 2b. It should be noted that the stress waves calculated in Figures. 2a and 2b account for Ni reflectivity (77%) [78]. The passing of these unloading tensile waves across the interface could drive interface failure, and as these waves propagate toward the bulk, their interaction could also drive spall failure. Here, Figure 2b illustrates the effects of a single-pulse; in the case of the two-pulse approach, another set of stress waves would be generated at the opposite surface.

Figure 2c displays the surface observation of the Ni coated Al_2O_3 samples under the single- and two-pulse laser approach for a range of laser fluences. Here, for a fixed spot size of $\sim 250 \mu\text{m}$, the laser fluence is adjusted by varying the pulse energy through a power attenuator. Once the sample was irradiated above a certain fluence threshold, sufficient tensile stress for interface separation was generated to induce Ni- Al_2O_3 adhesion failure due to the nucleation, growth, and coalescence of voids at the interface. Under SEM imaging, it can be seen that varying the laser fluence from 1,800 to 400 $\text{J}\cdot\text{m}^{-2}$ led to a reduction in the surface damage region, i.e., crater, from 230 μm to 56 μm , respectively—due to the reduction in tensile stress with decreasing laser fluence (see Figure 2b). The ejection of the Ni layer after interface debonding is most likely due to the outward propagation of the tensile stress waves and the radial compressive waves [79]. In the conventional single-pulse laser approach, interface failure takes place at the front surface only, however, introducing the secondary laser pulse led to failure at both the front and back surfaces. However, in both approaches, the surface features are similar highlighted with dangling Ni flakes and micro-voids on the Ni surface. Close inspection (as shown in Figure S1) of the surface morphology suggests that fracture under the dynamic tensile stress occurred mainly on the interface rather than on the Ni film indicating that the local adherence between Ni and Al_2O_3 might be weaker than the spall strength of Ni.

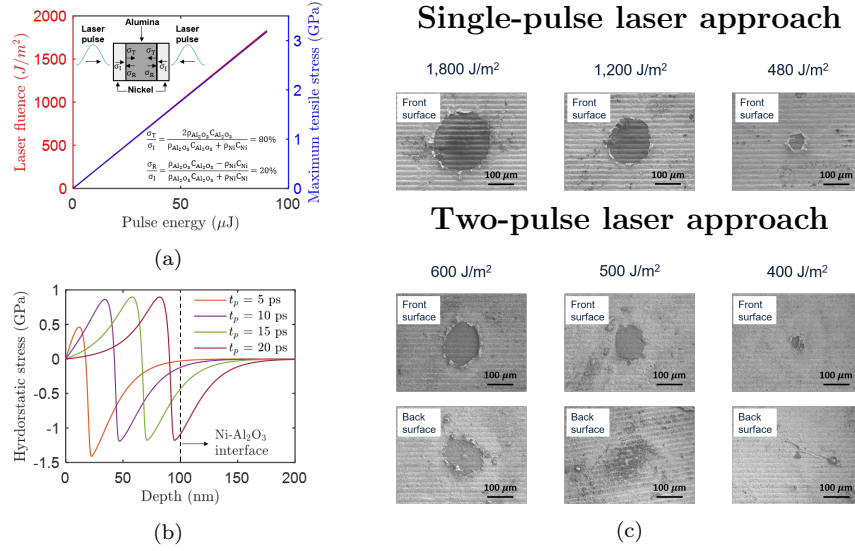


Figure 2: Illustration of the laser-induced stress wave propagation and failure mechanisms with analytical calculation of the (a) relationship between pulse energy, laser fluence, and maximum tensile stress for a fixed spot size of $\sim 250 \mu m$ and pulse duration of 350 fs, with an inset schematic of the Ni- Al_2O_3 structure depicting the incident, transmitted, and reflected stress waves and the corresponding ratios for transmitted/incident and reflected/incident stresses, (b) thermoelastic stress wave propagation across the Ni coating as a function of time with a fluence of $600 J \cdot m^{-2}$ and a pulse duration of 350 fs, and (c) SEM images of the surface features produced after single- (top) and two-pulse (bottom) laser illumination on the nickel coated Al_2O_3 samples displaying the front and back surfaces for a range of laser fluence between 1,800 to $400 J \cdot m^{-2}$. In these images, the Ni coating (visible as silver toned) is displayed with the underlying Al_2O_3 substrate exposed with varying degrees depending on the laser fluence.

To investigate the effects of single- and two-pulse laser approaches on the spall behavior of bulk Al_2O_3 , micro-CT analysis was conducted on two cases: a single-pulse laser with a fluence of $1,800 J \cdot m^{-2}$ and a two-pulse laser with a reduced fluence of $600 J \cdot m^{-2}$, as shown in Figs. 3a–d. A 3D pore structure was reconstructed using standard micro-CT segmentation and thresholding techniques [55, 56], where blue voxels represent smaller voids and red voxels indicate larger ones. In Figs. 3a and 3c, only pores with a volume larger than $50 \mu m^3$ are shown for better visualization. In the single-pulse approach (fluence: $1,800 J \cdot m^{-2}$), numerous voids were observed across the sample, with the larger ones concentrated near the front and back surfaces. In contrast, the two-pulse approach (fluence: $600 J \cdot m^{-2}$) resulted

in fewer voids, with the larger ones predominantly located near the sample’s center. The lower laser fluence in this approach led to fewer large voids being nucleated, as the generated tensile stress was lower (c.f., Figs. 3a and 3c). However, despite the lower number of voids, incipient spall failure still occurred in the two-pulse approach, as the interaction of unloading tensile waves enabled failure even at reduced fluence.

To further analyze the spall location and mechanisms, 2D slices of the samples were examined, as shown in Figs. 3b and 3d. For the single-pulse laser approach, clusters of voids were observed near the front and back surfaces. These voids formed primarily due to the passage of the unloading tensile wave (locations 1, 2, and 3 in Figure 3b) and the interaction of the reflected compressive wave with the unloading wave near the back surface (location 4 in Figure 3b). Additionally, pre-existing defects, wave reverberations, and partial reflections may have further contributed to the void distribution. In contrast, the two-pulse laser approach primarily induced central voids (locations 1, 2, 3, and 4 in Figure 3d). These voids were likely caused by the interaction of the two unloading tensile waves, which is characteristic of this method [28]. By incorporating a secondary pulse, the two-pulse approach shifts the spall location toward the sample center, as observed in Figure 3d. Furthermore, upon further analysis of the void morphology of the central void at location in one with the high-fidelity MD simulation in the inset figures in Figure 3d, it is clear to see that similarities can be drawn. The micro-CT scan reveals a crack pattern indicating some degree of propagation in an angled direction, suggesting an anisotropic effect similar to that observed in the MD simulations. Although crack initiation was not observed in the experiments, it can be inferred that the micro-crack propagated from an initial pore under a state of hydrostatic tensile stress (~ 1.8 GPa according to Figure 2b). This qualitative observation thus demonstrates that the macroscopic failure observed experimentally can be linked to the atomic-scale nano-void failure seen in the MD simulations.

Porosity analysis of the pristine sample (see Figure 1b) showed that 95% of pores had a volume below $3.58 \mu\text{m}^3$. After applying a size threshold to remove smaller pores, the pore volume distribution of the post-load samples is shown in Figure 3e. For single-pulse cases at fluences of 1,200 and 1,800 $\text{J} \cdot \text{m}^{-2}$, a similar trend was observed where the smallest and largest pore size were almost identical. Let us now focus on the two-pulse experiment also shown in Figure 3e. At $500 \text{J} \cdot \text{m}^{-2}$, no spall damage was observed, as the pore distribution remained similar to the pristine case with differences in the small

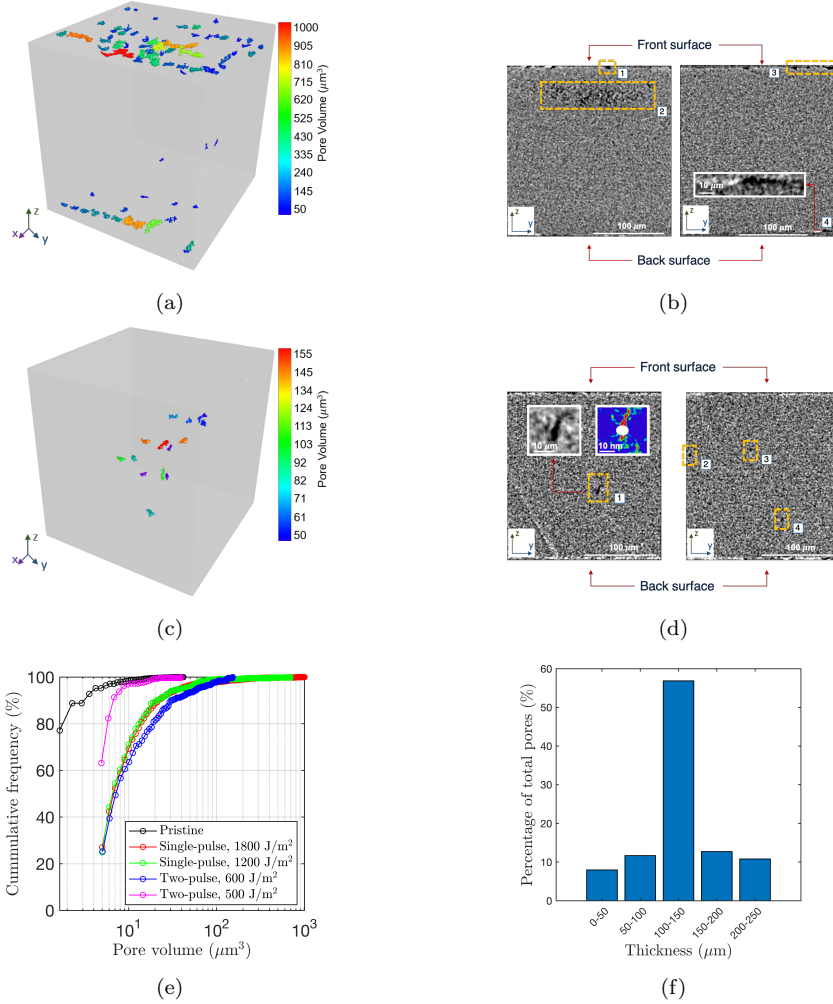


Figure 3: Illustration of spall failure in Al_2O_3 induced by the (a,b) single- (fluence: $1,800 \text{ J} \cdot \text{m}^{-2}$) and (c,d) two-pulse (fluence: $600 \text{ J} \cdot \text{m}^{-2}$) laser approaches, where (a, c) illustrates the 3D volume reconstructions from micro-CT scans with blue and red voxels indicating smaller and larger voids, (b, d) presents the 2D slices, also from micro-CT scans, highlighting failure locations associated with each approach, (e) displays the cumulative pore volume distribution comparing pristine and post-loaded samples under the single- ($1,800$ and $1,200 \text{ J} \cdot \text{m}^{-2}$) and two-pulse (600 and $500 \text{ J} \cdot \text{m}^{-2}$) laser approaches, and (f) describes the pore distribution for the two-laser setup at $600 \text{ J} \cdot \text{m}^{-2}$. The inset figure in (b) highlights a zoomed-in image of the largest void closest to the back surface, while (d) highlights a zoomed-in image of a central void and compares the crack morphology to that in Figure 5d at 5% strain.

pore sizes. Increasing the fluence to $600 \text{ J} \cdot \text{m}^{-2}$, we observed that the pore distribution matches quite neatly the single pulse experiments at 1200 and $1800 \text{ J} \cdot \text{m}^{-2}$. Noteworthy, the size of the largest pores is smaller for the two-laser setup due to the lower fluence of the single pulse ($600 \text{ J} \cdot \text{m}^{-2}$) and the decay effects of the shock pressure. Thus, the spall threshold for the two-pulse approach is estimated to be between 500 and $600 \text{ J} \cdot \text{m}^{-2}$. Comparing the single- and two-pulse cases at 1,800 and $600 \text{ J} \cdot \text{m}^{-2}$, respectively, the single-pulse case generated more numerous smaller voids compared to the two-pulse case but resulted in a lower 95th percentile pore volume ($38.1 \mu\text{m}^3$ vs. $59.8 \mu\text{m}^3$). However, the single-pulse approach produced a larger maximum pore volume ($1,000 \mu\text{m}^3$ vs. $150 \mu\text{m}^3$) because of the higher hydrostatic tensile stress.

Figure 3f shows the distribution of pore across the sample’s thickness for the two-laser setup at $600 \text{ J} \cdot \text{m}^{-2}$. Remarkably, we can observe that the pore location is concentrated near the center of the sample, where the interaction between release waves happened. In comparison, the pore distribution observed with the single-pulse setup (see Figure S2) reveals that, due to wave release and reflection, the spall planes appeared near the free surface of the samples, which is typical of the laser spall experiment. Moreover, pore distribution analysis (see Figure S2) showed two spall planes at $1,800 \text{ J} \cdot \text{m}^{-2}$, whereas only one spall plane near the illuminated surface at $1,200 \text{ J} \cdot \text{m}^{-2}$. This difference is due to the magnitude of the stress generated by the different fluence and the decay of the pressure with thickness. This highlights the two-pulse approach’s ability to induce spall failure at a specific location of the sample through the thickness, opening up potential applications to understand the spall failure of interfaces better.

3.2. Potential development and validation

Having established experimental insights into the spall behavior of Al_2O_3 , we now turn to molecular dynamics simulations to further investigate the material’s response at **ps** timescales and **nm** length scales. To enable accurate atomistic simulations, we developed an interatomic potential using the Allegro framework and first validate its accuracy against density functional theory (DFT) results. Figure 4a depicts the crystal structure of Al_2O_3 with atoms as spheres (nodes of the graph, i.e., n_i) and bonds as cylinders (edges of the graph, i.e., e_{ij}). Figures 4b–4c show parity plots of the validation dataset, demonstrating strong agreement between the DFT ground truth and the trained model predictions, as reflected by the high R^2 values (close

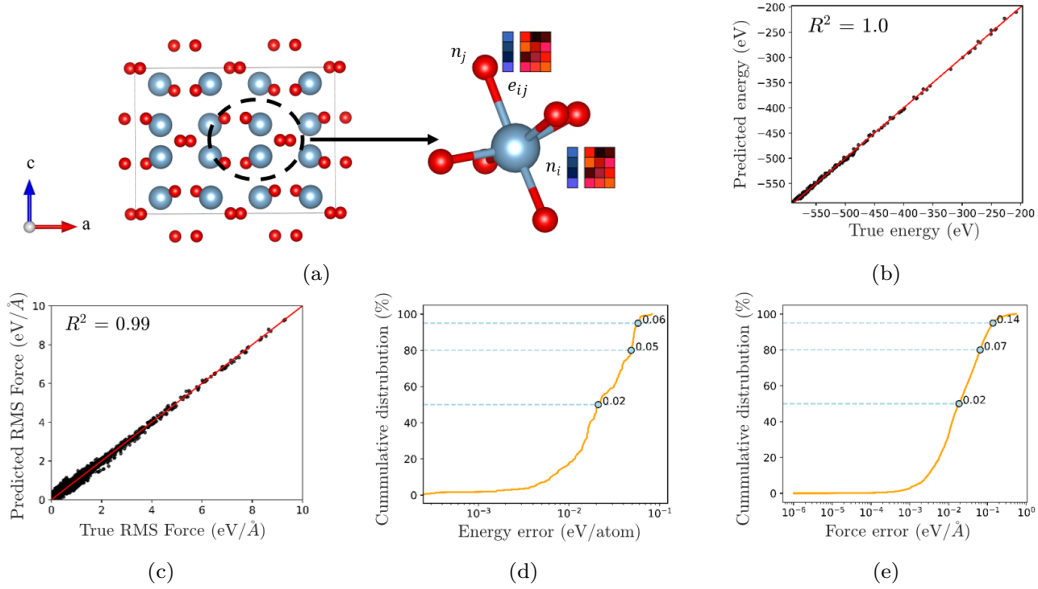


Figure 4: (a) Node (Al, O atoms) and edge (Al-O bond) update using the graph neural network. Here, the color codes for alumina atoms are red-oxygen and blue- aluminum. Here, the parity plots compare the Allegro-trained (predicted) model with DFT (true) for (b) energy and (c) root mean square (RMS) forces along with R^2 values; the cumulative distribution plots compare the absolute error (%) between the Allegro-trained model and DFT-relaxed alumina crystal in (d) energies and (e) forces.

to 1) for energy and force predictions. Here, the energy refers to the total potential energy of the alumina supercell, while the force represents the per-atom force acting on each atom. The cumulative distribution of the Allegro model errors, depicted in Figures 4d–4e, demonstrates the model’s accuracy, with horizontal dashed lines marking the 50th, 80th, and 95th percentiles of the energy and force errors. From these distributions, 50% of the data exhibit energy and force errors below 0.02 eV per atom and $0.02 \text{ eV} \cdot \text{\AA}^{-2}$; 80% fall below 0.05 eV per atom and $0.07 \text{ eV} \cdot \text{\AA}^{-2}$; and 95% remain below 0.06 eV per atom and $0.14 \text{ eV} \cdot \text{\AA}^{-2}$. The parity and cumulative plots indicate that the Allegro model predictions closely match DFT results, particularly given the stringent DFT training criteria (energy convergence: 0.001 meV , force convergence: $1 \text{ meV} \cdot \text{\AA}^{-1}$). Thus, these results demonstrate that the Allegro model achieves near-DFT-level accuracy, validating its reliability for atomistic simulations.

After validating the Allegro potential against DFT, we further assessed its

accuracy by comparing its predictions for key material properties of single-crystal alumina (elastic constants, cohesive energy, and vacancy formation energy) with those from two widely used interatomic potentials, COMB3 and ReaxFF. These values were also compared with DFT computed values available in the literature [80]. Table 1 highlights the accuracy of the Allegro potential in comparison to the selected reactive potentials. It should be noted that for Allegro potential, the predicted bulk modulus, calculated classically with deviatoric information [81, 82], is higher than the DFT and COMB3 calculated values but remarkably lower than ReaxFF.

Table 1: Comparison of elastic constants, bulk modulus (K), cohesive and vacancy formation energy among DFT [80], Allegro-MD, COMB3-MD, and ReaxFF-MD at ground state condition.

	DFT	Allegro-MD	COMB3-MD	ReaxFF-MD
C_{11} (GPa)	454	471	650	853
C_{22} (GPa)	394	376	472	878
C_{33} (GPa)	466	473	565	776
K (GPa)	232	290	270	508
E_{coh} (eV/atom)	-7.397	-7.398	-6.099	-6.014
O vacancy (eV/atom)	-7.343	-7.347	-6.110	-5.949
Al vacancy (eV/atom)	-7.296	-7.384	-6.037	-5.950
Al-O vacancy (eV/atom)	-7.312	-7.378	-6.052	-5.933

3.3. Nanovoid Simulations

To better illustrate the need for more accurate Al_2O_3 potentials, we provide a stress-strain and failure comparison between of Allegro, COMB3, and ReaxFF in Figure S3. From the comparison, it is evident that the stress values obtained from COMB3 are overpredicted, whereas the results from Allegro and ReaxFF are comparable. However, while Allegro predicts a brittle type of failure -as explained later-, ReaxFF predicts a ductile failure mode with phase transformation of the material. Let us now describe the behavior obtained with the Allegro potential. The initial phase of our analysis on the behavior of Al_2O_3 focuses on the relationship between the simulation cell volume and spall strength at strain rate of 10^8 s^{-1} . It is well established from the literature that cell size plays an impact on the accuracy of predicted physics [29, 30]. To explore this, simulations were conducted across

five different cell volumes: $V_{\text{cell}} = 10 \text{ nm}^3$ (128,398 atoms), 20 nm^3 (994,864 atoms), 30 nm^3 (3,248,624 atoms), 40 nm^3 (7,660,318 atoms), and 50 nm^3 (14,911,784 atoms). A fixed void volume of 0.4% was maintained across all cases to ensure consistency. The results, illustrated in Figure 5a, show that the spall strength becomes relatively insensitive to simulation cell size when V_{cell} reaches approximately 30 nm^3 . Additionally, the microstructural analysis, at 2% strain, in Figure 5a reveals that the 20 nm^3 cell size predicted a failure unlike the initial void deformation observed with other cell sizes. These findings suggest that a cell size of 30 nm^3 effectively minimizes periodic boundary effects during hydrostatic loading simulations. Therefore, we selected this cell size for subsequent investigations into the strain rate’s influence on Al_2O_3 behavior and to further analyze the failure mechanisms that lead to spallation.

Next, we proceed to describe the evolution of hydrostatic stress with strain under hydrostatic loading conditions for strain rates between 10^6 s^{-1} to 10^{10} s^{-1} . As shown in Figure 5b, the material initially undergoes a linear elastic response for all strain rates until reaching a critical volumetric strain, ϵ_f . Beyond this point, the material exhibits spall failure with anisotropic behavior, as evidenced from the calculated elastic constants in Table 1. As expected, the stress values were more pronounced along the **Y** direction (corresponding to the **22** direction), however, in all cases, brittle type of failure was consistently observed despite anisotropic effects [43, 83]. Here, the spall strength, i.e., the resistance of a material to fail under nanovoid growth, is characterized as the stress peak in Figure 5b. Both the spall strength and the critical strain exhibit a strong strain rate dependency, well-characterized by an exponential relationship. Specifically, the spall strength σ_{spall} can be described by an exponential model of the form $\sigma_{\text{spall}} = m \times e^{k\dot{\epsilon}}$, where m and k are fitting parameters, indicating that higher strain rates lead to significantly increased spall strength. For example, spall strength increases from 2.4 GPa at 10^6 s^{-1} to 10.1 GPa at 10^{10} s^{-1} . Similarly, the critical strain increases from 0.8% to 2.6% over the same range of strain rates. The stress-strain relationship demonstrates that the energy required to induce failure in Al_2O_3 increases with the strain rate. The energy required to cause failure rises from $14.5 \text{ MJ} \cdot \text{m}^{-3}$ at 10^6 s^{-1} to $170.5 \text{ MJ} \cdot \text{m}^{-3}$ at 10^{10} s^{-1} , highlighting the material’s increased resistance to failure under rapid deformation conditions. This increased resistance can be attributed to the inhibition of relaxation processes, such as bond breakage and crack propagation at higher rates, resulting in accumulated internal stresses.

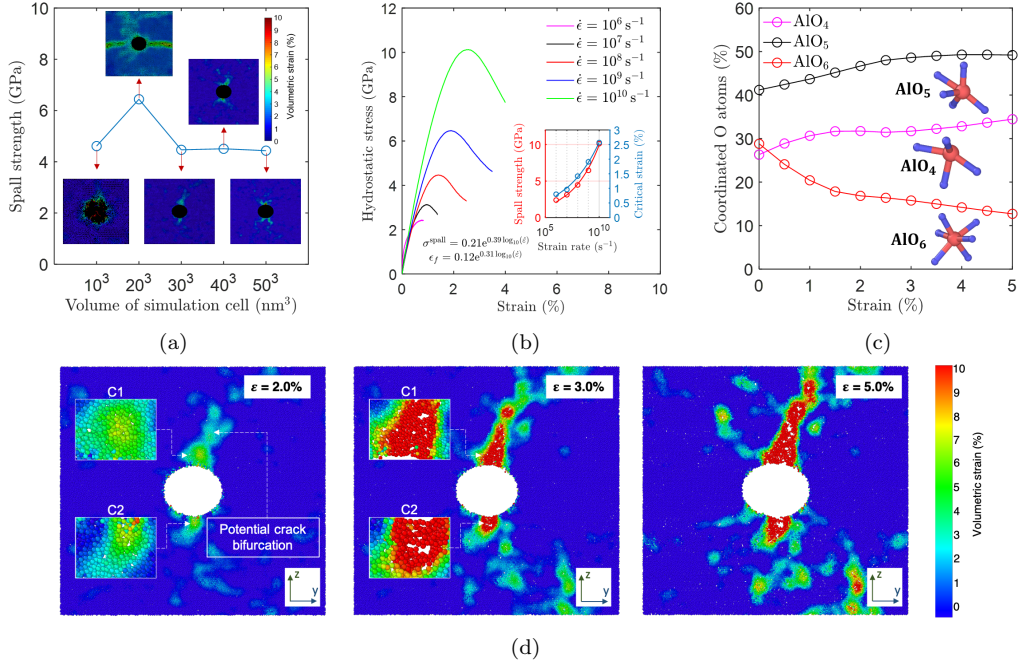


Figure 5: Molecular dynamics simulation of Al_2O_3 under hydrostatic loading with the following figures highlighting the (a) spall strength of five different simulation cells with a nanovoid corresponding to a void fraction 0.4% and the microstructure of each cell at 2% strain, (b) hydrostatic stress for different strain rates with an inset figure of the relationship between the spall strength, σ_{spall} , and critical strain, ϵ_f , with the strain rate, (c) change in coordination number of Al atoms with increasing strain and (d) spall behavior under a strain rate of 10^8 s^{-1} for a simulation cell with a volume of 30 nm^3 and a nano-void diameter of 6 nm.

We proceed to explain in detail the spall failure behavior of Al_2O_3 under hydrostatic loading. It should be noted that despite the differences in spall strength and critical strain, the failure mechanism is invariant with respect to the strain rate. As such, the spall behavior discussed here corresponds to 10^8 s^{-1} . Prior to reaching the critical strain ($= 1.4\%$), the Al-O bonds are stretched elastically without failure. However, upon reaching it, bond breakage starts to take place very close to the nano-void as shown in Figure S4. Due to the presence of the nanovoid, stress concentration exists leading to larger stress states closer to the nanovoid which is the prime site for failure initiation as seen here, and reported in the literature [84, 85, 86]. An influential factor indicating bond breakage is the coordination number, which

corresponds to the number of bonds per each Al and O atom. Here, we focus on the Al-O bonds, as they were far more in number in comparison to Al-Al and O-O bonds. Figure 5c illustrates the change in the coordination number of Al atoms, where we track 4-coordinated (AlO_4), 5-coordinated (AlO_5), and 6-coordinated (AlO_6) Al atoms with increasing strain. Here, it can be seen that with increasing strain the total number of AlO_6 bonds reduces to AlO_4 and AlO_5 indicating an increase in bond breakage. Hence with the increase in tension beyond the critical strain, Al-O interatomic bonds tend to cleave leading to initial brittle spall failure.

The coalescence of these broken bonds form micro-cracks, and this can be seen in Figure 5d, when the strain reaches 2%. Figure 5d illustrates a series of 2D slices, along the **YZ** plane, of the brittle spall failure originating from the nanovoid. Here, we can see the formation of two localized regions (highlighted by the increased volumetric strain) close to the nanovoid where micro-cracks formation takes place (labeled as C1 and C2). In the figure, the red regions represent atoms that experienced $\epsilon \rightarrow 10.0\%$, and blue atoms $\epsilon \rightarrow 0.0\%$. These localized regions, C1 and C2, are created as a result of the increased displacement of atoms due to stress concentration effects. However, it is evident that some degree of anisotropy took place leading to specific orientation of these microcracks at an angle from the nanovoid. Furthermore, these regions are also characterized with vacancies arising due to the bond breakage (see Figure S4). It can be seen that when $\epsilon = 3.0\%$, with the increase in tension, atoms in C1 and C2 experience large volumetric strain leading to the nucleation of voids. Interestingly, when comparing the microstructure at $\epsilon = 2.0\%$ and 3.0% that C1, instead of bifurcating, expanded into a larger crack as it was more energetically favorable to do so. Lastly, at $\epsilon = 5.0\%$, it can be seen that while C2 experienced a crack arrest, C1 propagates to the edges of the periodic simulation cell. However, due to the anisotropic behavior of Al_2O_3 , the failure behavior is dependent on the orientation (cf., Figure S5). Overall, it can be seen that the governing mechanisms behind the brittle failure of Al_2O_3 under high-strain-rate hydrostatic loading are bond breakage, micro-crack formation and coalescence, crack propagation, and crack bifurcation. As these cracks grow and propagate, they eventually coalesce to generate a free surface as shown in Figure S6. It is evident that the initial nanovoid acted as the prime site for failure, as multiple microcracks formed close to the vicinity to then expand and form a spall plane. These findings compare very well with existing experimental findings [16, 18, 87]. Furthermore, the nanovoid size impacts

both the degree of failure and spall strength as can be found in Figure S7.

3.4. Spall strength of alumina

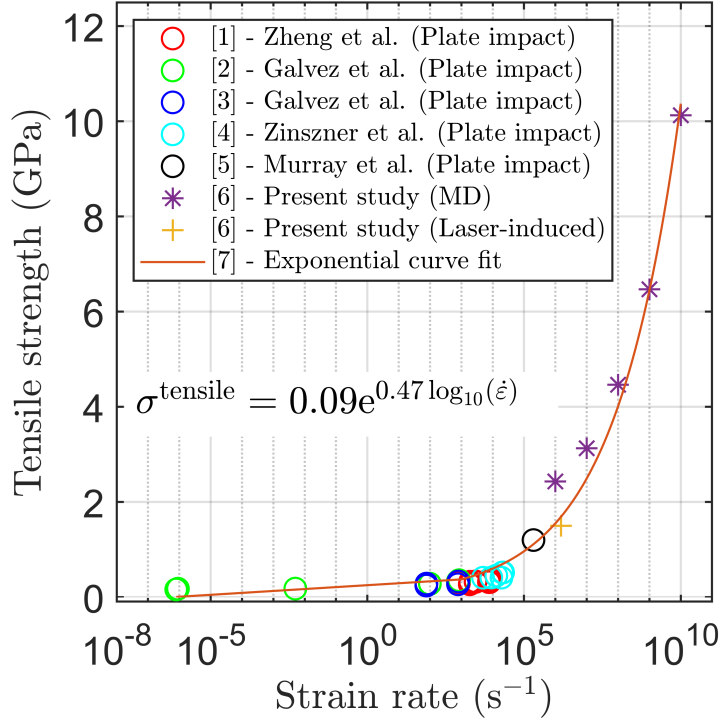


Figure 6: Comparison of the spall strength for alumina for different strain rates. Data values combine plate impact experiments, the two-laser setup estimation and molecular dynamics simulations with the potential developed in this work.

Figure 6 displays the tensile strength trend with strain rate for Al_2O_3 across a range from 10^{-7} s^{-1} to 10^{10} s^{-1} with respect to the literature, MD simulations, and the laser-induced spall experiment. The spall strength, i.e., essentially the tensile strength under high-strain-rates, exhibits good agreement with MD simulations and literature data, as evidenced by the exponential curve fit. Experimental studies in the literature have been limited to strain rates up to 10^5 s^{-1} [88, 89, 90, 15, 17]. Under the single-pulse approach, prior studies have shown that spall strength can be inferred from the spall thickness, i.e., the distance of spall failure from the back surface [57, 58, 28]. Here, location 4 in Figure 3b corresponds to the largest void

nearest to the back surface ($\sim 800 \mu^3$, see Figure S2), with a spall thickness of $\sim 8 \mu\text{m}$. The spall thickness β can be related to the shock velocity V_s , sample thickness ω , bulk sound speed c_0 , and pulse duration τ with the following relationship [28]:

$$V_s = \frac{c_0\omega + \beta c_0}{\beta - \omega + \tau c_0} \quad (1)$$

With $\omega = 250 \mu\text{m}$, $\tau = 350 \text{ fs}$, $c_0 = 7,455 \text{ m} \cdot \text{s}^{-1}$, the calculated V_s is $796 \text{ m} \cdot \text{s}^{-1}$. Using the Hugoniot relationship, the calculated particle velocity $V_p = (V_s - c_0)/\lambda = 387 \text{ m} \cdot \text{s}^{-1}$ and shock pressure $P_o = \rho V_s V_p = 12 \text{ GPa}$. Here, the Hugoniot slope λ is 1.31 [77]. For a triangular pressure pulse, the spall strength and strain rate can be expressed as $\sigma_{\text{spall}} = 2(P_o - \rho c_0 V_p)$ and $\dot{\epsilon} = U_p/L$, respectively [57]. From β , the spall strength in the Al_2O_3 sample is estimated at $\sim 1.5 \text{ GPa}$, with an associated strain rate of $1.5 \times 10^6 \text{ s}^{-1}$. While the experimentally estimated spall strength is lower than the MD-predicted value ($\sigma_{\text{spall}}^{\text{experiment}} = 1.5 \text{ GPa}$ and $\sigma_{\text{spall}}^{\text{MD}} = 2.4 \text{ GPa}$), this difference is expected, as MD simulations do not account for factors such as compression, impurities, and other complexities known to influence spall strength [16, 17, 18, 19, 20, 21].

4. Conclusions

In this study, the spall behavior of Al_2O_3 was examined using a combined approach that integrates high-fidelity informed molecular dynamics simulations with femtosecond laser-induced experiments. An interatomic potential for Al_2O_3 was developed by training an equivariant neural network model on an extensive dataset generated from density-functional theory calculations. The molecular dynamics simulations explored a range of strain rates from 10^6 s^{-1} to 10^{10} s^{-1} , while the experiments were conducted at a strain rate on the order of 10^6 s^{-1} , with a maximum laser pulse energy of $90 \mu\text{J}$. To induce spall conditions, both single- (illumination of the front surface only) and two-pulse (illumination of both front and back surfaces) laser approaches were employed after coating a thin layer of nickel to the Al_2O_3 samples to enhance energy absorption. The main findings of this investigation are as follows:

- The surface response of the Ni-coated Al_2O_3 sample to single- and two-pulse laser approaches demonstrated that sufficient tensile stress

induced Ni-Al₂O₃ interface failure when the laser fluence surpassed a threshold. SEM analysis revealed a reduction in damage region size with decrease in laser fluence, correlating with decreased tensile stress (c.f., Figures 2a and 2c). The dynamic tensile stress primarily caused fracture at the interface rather than within the Ni film itself (see Figure S1), indicating that the local adhesion between Ni and Al₂O₃ was weaker than the spall strength of Ni.

- To investigate the impact of single- and two-pulse laser approaches on the spall behavior of bulk Al₂O₃, micro-CT analysis was conducted on samples loaded with (a) single-pulse laser with a fluence of 1,800 J · m⁻² and (b) two-pulse approach with a reduced fluence of 600 J · m⁻² (see Figures 3a and 3c). The 3D volume reconstructions revealed that the two-pulse approach exhibited fewer voids predominantly, however, despite this, spallation conditions were still achieved. The single-pulse approach generated voids primarily close to the front and back surfaces, while the two-pulse approach produced voids at the sample’s center (see Figures 3b and 3d). The estimated strain rate of 1.5×10^7 s⁻¹ and spall strength of 1.5 GPa under the single-pulse case were consistent with the molecular dynamics simulations and the literature [88, 89, 90, 15, 17] (see Figure 3f).
- MD simulations demonstrate that Al₂O₃ exhibits strain rate-dependent spall behavior under hydrostatic loading, with spall strength and critical strain increasing as the strain rate rises, as shown in Figure 5b. The exponential relationship between spall strength and strain rate, along with the increase in energy required for failure, points to the material’s enhanced resistance due to suppressed relaxation processes and accumulated internal stresses resulting in a higher threshold for failure with increased strain rate.
- MD simulations indicate that beyond the critical strain, bond breakage initiates near a nanovoid (see Figure S4), leading to brittle failure. The coordination number analysis indicates the transition from AlO₆ to AlO₄ and AlO₅ with increasing strain, signifying bond cleavage (see Figure 5c). This bond breakage forms micro-cracks that coalesce and propagate, forming larger cracks that eventually develops to form a spall plane (see Figures 5d, and S5—S6). The failure mechanism is

influenced by stress concentration, anisotropic behavior, and nanovoid size, with the literature validating these observations [16, 18, 87].

Thus, our findings shed light on the spall behavior of Al_2O_3 under high-strain-rates. The study highlights the unique advantages of femtosecond laser-induced spall approaches, particularly the two-pulse laser approach, which effectively reduces the laser fluence required to achieve sufficient spall conditions. This study shows a comparison between the behavior of shocked specimens under single and two-pulse experiments with femtosecond laser-induced spall approaches. Remarkably, we illustrated the ability of the two-pulse experiment to develop voids in the middle of the sample due to shock wave interactions. Our work opens up the possibility to further investigate the shock behavior of materials and interfaces that cannot be accessed through traditional experiments such as plate impact by controlling the spall failure location. Moreover, this approach enables the characterization of spall behavior at extremely high-strain-rates, surpassing the limitations of traditional plate-impact methods. Coupling these experiments with high-fidelity molecular dynamics simulations allows for understanding the failure mechanisms that take place at **fs–ns** time and **nm** spatial scales. Hence, the femtosecond laser-induced spall approach serves as a promising tool for analyzing the spall behavior of ceramics under conditions previously inaccessible with conventional techniques, paving the way for more efficient and high-throughput experimental methods.

Code availability

The code developed to analytically calculate the thermoelastic stress and prepare the DFT simulations and data set can be found at:

- <https://github.com/mewael-isiet/analytical-thermoelastic-wave>
- <https://github.com/MusannaGalib/AtomProNet>

CRedit author statement

Mewael Isiet: Methodology, Software, Validation, Formal analysis, Investigation, Data Curation, Visualization, Writing - Original Draft, Writing - Review & Editing. **Musanna Galib**: Methodology, Software, Validation, Data Curation, Writing - Original Draft, Writing - Review & Editing.

Jerry I. Dadap: Methodology, Supervision, Writing - Review & Editing. **Yunhuan Xiao:** Methodology, Writing - Review & Editing. **Ziliang Ye:** Resources, Writing - Review & Editing. **Mauricio Ponga:** Conceptualization, Methodology, Software, Resources, Project administration, Funding acquisition, Supervision, Writing - Review & Editing.

Data availability

Data will be made available on request.

Acknowledgements

We acknowledge the support of the New Frontiers in Research Fund (NFRFE-2019-01095) and the Natural Sciences and Engineering Research Council of Canada (NSERC) through the Discovery Grant and ALLRP 560447-2020 grants. This research was supported through high-performance computational resources and services provided by Advanced Research Computing at the University of British Columbia and the Digital Research Alliance of Canada. We acknowledge the support of Canada Foundation for Innovation (CFI). Z.Y. was supported by the Canada Research Chairs Program.

References

- [1] W. A. Gooch, “An overview of ceramic armor applications,” *Ceramic transactions*, vol. 134, pp. 3–21, 2002.
- [2] E. Medvedovski, “Ballistic performance of armour ceramics: Influence of design and structure. part 2,” *Ceramics International*, vol. 36, p. 2117–2127, Sept. 2010.
- [3] M. V. Silva, D. Stainer, H. A. Al-Qureshi, O. R. K. Montedo, and D. Hotza, “Alumina-based ceramics for armor application: Mechanical characterization and ballistic testing,” *Journal of Ceramics*, vol. 2014, p. 1–6, Jan. 2014.
- [4] W. Liu, Z. Chen, X. Cheng, Y. Wang, A. R. Amankwa, and J. Xu, “Design and ballistic penetration of the ceramic composite armor,” *Composites Part B: Engineering*, vol. 84, p. 33–40, Jan. 2016.

- [5] E. Medvedovski, "Ballistic performance of armour ceramics: Influence of design and structure. part 1," *Ceramics International*, vol. 36, p. 2103–2115, Sept. 2010.
- [6] E. Medvedovski, "Alumina–mullite ceramics for structural applications," *Ceramics International*, vol. 32, p. 369–375, Jan. 2006.
- [7] G. J. Appleby-Thomas, K. Jaansalu, A. Hameed, J. Painter, J. Shackel, and J. Rowley, "A comparison of the ballistic behaviour of conventionally sintered and additively manufactured alumina," *Defence Technology*, vol. 16, p. 275–282, Apr. 2020.
- [8] A. B. Dresch, J. Venturini, S. Arcaro, O. R. Montedo, and C. P. Bergmann, "Ballistic ceramics and analysis of their mechanical properties for armour applications: A review," *Ceramics International*, vol. 47, p. 8743–8761, Apr. 2021.
- [9] J. Reaugh, A. Holt, M. Welkins, B. Cunningham, B. Hord, and A. Kusubov, "Impact studies of five ceramic materials and pyrex," *International Journal of Impact Engineering*, vol. 23, p. 771–782, Dec. 1999.
- [10] A. Krell and E. Strassburger, "Order of influences on the ballistic resistance of armor ceramics and single crystals," *Materials Science and Engineering: A*, vol. 597, p. 422–430, Mar. 2014.
- [11] N. D. Andraskar, G. Tiwari, and M. D. Goel, "Impact response of ceramic structures - a review," *Ceramics International*, vol. 48, p. 27262–27279, Oct. 2022.
- [12] M. E. Backman and W. Goldsmith, "The mechanics of penetration of projectiles into targets," *International Journal of Engineering Science*, vol. 16, p. 1–99, Jan. 1978.
- [13] C. Yungwirth, J. O'Connor, A. Zakraysek, V. S. Deshpande, and H. N. G. Wadley, "Explorations of hybrid sandwich panel concepts for projectile impact mitigation," *Journal of the American Ceramic Society*, vol. 94, Apr. 2011.

- [14] A. Serjouei, R. Chi, I. Sridhar, and G. E. Tan, “Empirical ballistic limit velocity model for bi-layer ceramic–metal armor,” *International Journal of Protective Structures*, vol. 6, p. 509–527, Sept. 2015.
- [15] J. Zinszner, B. Erzar, P. Forquin, and E. Buzaud, “Dynamic fragmentation of an alumina ceramic subjected to shockless spalling: An experimental and numerical study,” *Journal of the Mechanics and Physics of Solids*, vol. 85, p. 112–127, Dec. 2015.
- [16] L. H. L. Louro and M. A. Meyers, “Effect of stress state and microstructural parameters on impact damage of alumina-based ceramics,” *Journal of Materials Science*, vol. 24, p. 2516–2532, July 1989.
- [17] N. H. Murray, N. K. Bourne, Z. Rosenberg, and J. E. Field, “The spall strength of alumina ceramics,” *Journal of Applied Physics*, vol. 84, p. 734–738, July 1998.
- [18] N. K. Bourne, “The onset of damage in shocked alumina,” *Proceedings of the Royal Society of London. Series A: Mathematical, Physical and Engineering Sciences*, vol. 457, p. 2189–2205, Sept. 2001.
- [19] I. Gurlitsky, E. Zaretsky, S. Kalabukhov, M. P. Dariel, and N. Frage, “Dynamic compressive and tensile strengths of spark plasma sintered alumina,” *Journal of Applied Physics*, vol. 115, June 2014.
- [20] S. Hayun, E. Ionash, S. Kalabukhov, N. Frage, and E. Zaretsky, “Strength of ceramic–metal joints measured in planar impact experiments,” *Journal of Materials Science*, vol. 53, p. 8211–8220, Feb. 2018.
- [21] A. Lebar, R. Aguiar, A. Oddy, and O. E. Petel, “Particle surface effects on the spall strength of particle-reinforced polymer matrix composites,” *International Journal of Impact Engineering*, vol. 150, p. 103801, Apr. 2021.
- [22] J. Lankford, “Compressive strength and microplasticity in polycrystalline alumina,” *Journal of Materials Science*, vol. 12, p. 791–796, Apr. 1977.
- [23] D. D. Mallick, S. E. Prameela, D. Ozturk, C. L. Williams, M. Kang, G. M. Valentino, J. T. Lloyd, J. W. Wilkerson, T. P. Weihs, and K. Ramesh, “Spall strength in alloyed magnesium: A compendium of

- research efforts from the cmede 10-year effort,” *Mechanics of Materials*, vol. 162, p. 104065, Nov. 2021.
- [24] R. Thevamaran, O. Lawal, S. Yazdi, S.-J. Jeon, J.-H. Lee, and E. L. Thomas, “Dynamic creation and evolution of gradient nanostructure in single-crystal metallic microcubes,” *Science*, vol. 354, p. 312–316, Oct. 2016.
- [25] C. Griesbach, J. Cai, S.-J. Jeon, and R. Thevamaran, “Synergistic strength and toughness through impact-induced nanostructural evolutions in metals,” *Extreme Mechanics Letters*, vol. 62, p. 102037, Aug. 2023.
- [26] D. D. Mallick and K. Ramesh, “Dynamic fragmentation of boron carbide using laser-driven flyers,” *International Journal of Impact Engineering*, vol. 136, p. 103416, Feb. 2020.
- [27] D.-Y. Wu, C. Miao, C. S. DiMarco, K. Ramesh, and T. C. Hufnagel, “Microstructural effects on the spall failure of 7085 aluminum alloy,” *Materials Science and Engineering: A*, vol. 866, p. 144674, Feb. 2023.
- [28] M. Isiet, Y. Xiao, J. I. Dadap, Z. Ye, and M. Ponga, “Femtosecond two-pulse laser approach for spall failure in thin foils,” *arXiv preprint arXiv:2412.04762*, 2024.
- [29] M. Ponga, A. A. Ramabathiran, K. Bhattacharya, and M. Ortiz, “Dynamic behavior of nano-voids in magnesium under hydrostatic tensile stress,” *Modelling and Simulation in Materials Science and Engineering*, vol. 24, p. 065003, July 2016.
- [30] C. Grégoire and M. Ponga, “Nanovoid failure in magnesium under dynamic loads,” *Acta Materialia*, vol. 134, p. 360–374, Aug. 2017.
- [31] M. V. Shugaev and L. V. Zhigilei, “Thermodynamic analysis and atomistic modeling of subsurface cavitation in photomechanical spallation,” *Computational Materials Science*, vol. 166, p. 311–317, Aug. 2019.
- [32] D. S. Ivanov and L. V. Zhigilei, “Combined atomistic-continuum modeling of short-pulse laser melting and disintegration of metal films,” *Physical Review B*, vol. 68, Aug. 2003.

- [33] J.-L. Shao, P. Wang, A.-M. He, R. Zhang, and C.-S. Qin, “Spall strength of aluminium single crystals under high strain rates: Molecular dynamics study,” *Journal of Applied Physics*, vol. 114, p. 173501, Nov. 2013.
- [34] S. Galitskiy, D. S. Ivanov, and A. M. Dongare, “Dynamic evolution of microstructure during laser shock loading and spall failure of single crystal Al at the atomic scales,” *Journal of Applied Physics*, vol. 124, Nov. 2018.
- [35] S. J. Fensin, E. K. Cerreta, G. T. G. III, and S. M. Valone, “Why are some interfaces in materials stronger than others?,” *Scientific Reports*, vol. 4, June 2014.
- [36] Q.-L. Xiong, Z. Li, and T. Kitamura, “Effect of crystal orientation on femtosecond laser-induced thermomechanical responses and spallation behaviors of copper films,” *Scientific Reports*, vol. 7, Aug. 2017.
- [37] D. Thürmer, S. Zhao, O. R. Deluigi, C. Stan, I. A. Alhafez, H. M. Urbassek, M. A. Meyers, E. M. Bringa, and N. Gunkelmann, “Exceptionally high spallation strength for a high-entropy alloy demonstrated by experiments and simulations,” *Journal of Alloys and Compounds*, vol. 895, p. 162567, Feb. 2022.
- [38] W. Li, S. Chen, Z. Aitken, and Y.-W. Zhang, “Shock-induced deformation and spallation in CoCrFeMnNi high-entropy alloys at high strain-rates,” *International Journal of Plasticity*, vol. 168, p. 103691, Sept. 2023.
- [39] M. S. Nitol, S. Adibi, C. D. Barrett, and J. W. Wilkerson, “Solid solution softening in dislocation-starved Mg–Al alloys,” *Mechanics of Materials*, vol. 150, p. 103588, Nov. 2020.
- [40] X. Yang, S. Xu, and L. Liu, “The shock response and spall mechanism of Mg–Al–Zn alloy: Molecular dynamics study,” *Acta Mechanica Solida Sinica*, vol. 35, p. 495–503, Feb. 2022.
- [41] B. Chen, Y. Li, D. Şopu, J. Eckert, and W. Wu, “Molecular dynamics study of shock-induced deformation phenomena and spallation failure in Ni-based single crystal superalloys,” *International Journal of Plasticity*, vol. 162, p. 103539, Mar. 2023.

- [42] J. Chang, Z. Chen, and J. D. Hogan, “Molecular dynamics simulations correlating mechanical property changes of alumina with atomic voids under triaxial tension loading,” *Modelling*, vol. 4, p. 211–223, May 2023.
- [43] C. Zhang, R. K. Kalia, A. Nakano, P. Vashishta, and P. S. Branicio, “Deformation mechanisms and damage in α -alumina under hypervelocity impact loading,” *Journal of Applied Physics*, vol. 103, Apr. 2008.
- [44] W. Li and X. Yao, “The spallation of single crystal sic: The effects of shock pulse duration,” *Computational Materials Science*, vol. 124, p. 151–159, Nov. 2016.
- [45] W. Li, X. Yao, P. Branicio, X. Zhang, and N. Zhang, “Shock-induced spall in single and nanocrystalline sic,” *Acta Materialia*, vol. 140, p. 274–289, Nov. 2017.
- [46] P. Vashishta, R. K. Kalia, A. Nakano, and J. P. Rino, “Interaction potential for aluminum nitride: A molecular dynamics study of mechanical and thermal properties of crystalline and amorphous aluminum nitride,” *Journal of Applied Physics*, vol. 109, Feb. 2011.
- [47] K. Choudhary, T. Liang, A. Chernatynskiy, S. R. Phillpot, and S. B. Sinnott, “Charge optimized many-body (COMB) potential for al₂o₃materials, interfaces, and nanostructures,” *Journal of Physics: Condensed Matter*, vol. 27, p. 305004, July 2015.
- [48] S. Hong and A. C. T. van Duin, “Atomistic-scale analysis of carbon coating and its effect on the oxidation of aluminum nanoparticles by reaxff-molecular dynamics simulations,” *The Journal of Physical Chemistry C*, vol. 120, p. 9464–9474, Apr. 2016.
- [49] S. Wan, R. C. Sinclair, and P. V. Coveney, “Uncertainty quantification in classical molecular dynamics,” *Philosophical Transactions of the Royal Society A: Mathematical, Physical and Engineering Sciences*, vol. 379, Mar. 2021.
- [50] N. Piroozan and N. Kumar, “Enabling performant thermal conductivity modeling with DeePMD and LAMMPS on CPUs,” in *Proceedings of the SC '23 Workshops of The International Conference on High Performance Computing, Network, Storage, and Analysis*, SC-W 2023, ACM, Nov. 2023.

- [51] S. Naserifar, L. Liu, W. A. Goddard, T. T. Tsotsis, and M. Sahimi, “Toward a process-based molecular model of SiC membranes. 1. development of a reactive force field,” *The Journal of Physical Chemistry C*, vol. 117, p. 3308–3319, Feb. 2013.
- [52] S. Batzner, A. Musaelian, L. Sun, M. Geiger, J. P. Mailoa, M. Kornbluth, N. Molinari, T. E. Smidt, and B. Kozinsky, “E(3)-equivariant graph neural networks for data-efficient and accurate interatomic potentials,” *Nature Communications*, vol. 13, May 2022.
- [53] A. Musaelian, S. Batzner, A. Johansson, L. Sun, C. J. Owen, M. Kornbluth, and B. Kozinsky, “Learning local equivariant representations for large-scale atomistic dynamics,” *Nature Communications*, vol. 14, Feb. 2023.
- [54] Comet Technologies Canada Inc., “Dragonfly 2024.1,” 2024. Software available at <https://dragonfly.comet.tech/>.
- [55] F. Košek, J. Dudák, V. Tymlová, J. Žemlička, D. Řimnáčová, and J. Jehlička, “Evaluation of pore-fracture microstructure of gypsum rock fragments using micro-ct,” *Micron*, vol. 181, p. 103633, June 2024.
- [56] C. Desrosiers, M. Letenneur, F. Bernier, N. Piché, B. Provencher, F. Cheriet, F. Guibault, and V. Brailovski, “Automated porosity segmentation in laser powder bed fusion part using computed tomography: a validity study,” *Journal of Intelligent Manufacturing*, Jan. 2024.
- [57] I. Gilath, S. Eliezer, M. Dariel, L. Kornblit, and T. Bar-Noy, “Laser induced spall in aluminum and copper,” *Journal de Physique Colloques*, vol. 49, no. C3, pp. C3–191, 1988.
- [58] H. Jarmakani, B. Maddox, C. Wei, D. Kalantar, and M. Meyers, “Laser shock-induced spalling and fragmentation in vanadium,” *Acta Materialia*, vol. 58, p. 4604–4628, Aug. 2010.
- [59] W. Kohn and L. J. Sham, “Self-consistent equations including exchange and correlation effects,” *Phys. Rev.*, vol. 140, pp. A1133–A1138, Nov 1965.
- [60] P. Hohenberg and W. Kohn, “Inhomogeneous electron gas,” *Phys. Rev.*, vol. 136, pp. B864–B871, Nov 1964.

- [61] G. Kresse and J. Furthmüller, “Efficiency of ab-initio total energy calculations for metals and semiconductors using a plane-wave basis set,” *Computational Materials Science*, vol. 6, no. 1, pp. 15–50, 1996.
- [62] J. P. Perdew, K. Burke, and M. Ernzerhof, “Generalized gradient approximation made simple,” *Phys. Rev. Lett.*, vol. 77, pp. 3865–3868, Oct 1996.
- [63] G. Kresse and D. Joubert, “From ultrasoft pseudopotentials to the projector augmented-wave method,” *Phys. Rev. B*, vol. 59, pp. 1758–1775, Jan 1999.
- [64] M. Galib, O. K. Orhan, and M. Ponga, “Engineering chemo-mechanical properties of zn surfaces via alucone coating,” *The Journal of Physical Chemistry C*, vol. 127, no. 5, pp. 2481–2492, 2023.
- [65] M. Galib, M. Isiet, and M. Ponga, “Atompronet: Data flow to and from machine learning interatomic potentials in materials science,” *arXiv preprint arXiv:2501.14039*, 2025.
- [66] M. Geiger and T. Smidt, “e3nn: Euclidean neural networks,” *arXiv preprint arXiv:2207.09453*, 2022.
- [67] D. Hendrycks and K. Gimpel, “Gaussian error linear units (GELUs),” *arXiv preprint arXiv:1606.08415*, 2023.
- [68] D. P. Kingma and J. Ba, “Adam: A method for stochastic optimization,” *arXiv preprint arXiv:1412.6980*, 2017.
- [69] A. Paszke, S. Gross, F. Massa, A. Lerer, J. Bradbury, G. Chanan, T. Killeen, Z. Lin, N. Gimeshain, L. Antiga, A. Desmaison, A. Kopf, E. Yang, Z. DeVito, M. Raison, A. Tejani, S. Chilamkurthy, B. Steiner, L. Fang, J. Bai, and S. Chintala, “PyTorch: An imperative style, high-performance deep learning library,” in *Advances in Neural Information Processing Systems* (H. Wallach, H. Larochelle, A. Beygelzimer, F. d'Alché-Buc, E. Fox, and R. Garnett, eds.), vol. 32, Curran Associates, Inc., 2019.
- [70] A. P. Thompson, H. M. Aktulga, R. Berger, D. S. Bolintineanu, W. M. Brown, P. S. Crozier, P. J. in 't Veld, A. Kohlmeyer, S. G. Moore, T. D. Nguyen, R. Shan, M. J. Stevens, J. Tranchida, C. Trott, and S. J.

- Plimpton, “LAMMPS - a flexible simulation tool for particle-based materials modeling at the atomic, meso, and continuum scales,” *Computer Physics Communications*, vol. 271, p. 108171, 2022.
- [71] A. Jain, S. Ong, G. Hautier, W. Chen, W. D. Richards, S. Dacek, S. Cholia, D. Gunter, D. Skinner, G. Ceder, and K. A. Persson, “Commentary: The materials project: A materials genome approach to accelerating materials innovation,” *APL Materials*, vol. 1, July 2013.
- [72] J.-F. Lin, O. Degtyareva, C. T. Prewitt, P. Dera, N. Sata, E. Gregoryanz, H. Mao, and R. J. Hemley, “Crystal structure of a high-pressure/high-temperature phase of alumina by in situ X-ray diffraction,” *Nature Materials*, vol. 3, p. 389–393, May 2004.
- [73] B. Xu, H. Stokes, and J. Dong, “First-principles calculation of kinetic barriers and metastability for the corundum-to-Rh₂O₃(II) transition in Al₂O₃,” *Journal of Physics: Condensed Matter*, vol. 22, p. 315403, July 2010.
- [74] G. Martyna, D. Tobias, and M. Klein, “Constant pressure molecular dynamics algorithms,” *The Journal of chemical physics*, vol. 101, no. 5, pp. 4177–4189, 1994.
- [75] M. Allen and D. Tildesley, *Computer simulation of liquids*. Oxford University Press, 2017.
- [76] A. Stukowski, “Visualization and analysis of atomistic simulation data with ovito—the open visualization tool,” *Modelling and simulation in materials science and engineering*, vol. 18, no. 1, p. 015012, 2009.
- [77] W. Reinhart and L. Chhabildas, “Strength properties of coors ad995 alumina in the shocked state,” *International Journal of Impact Engineering*, vol. 29, p. 601–619, Dec. 2003.
- [78] P. Johnson and R. Christy, “Optical constants of transition metals: Ti, V, Cr, Mn, Fe, Co, Ni, and Pd,” *Physical Review B*, vol. 9, p. 5056–5070, June 1974.
- [79] T. de Ressaiguier, X. Milhet, V. Labussière, E. Barraud, L. Signor, and J. Baillargeat, “Laser-driven shocks to explore the effects of aging on the

- adhesion of silver sintered on copper substrate,” *Journal of Adhesion Science and Technology*, vol. 36, p. 1346–1363, Sept. 2021.
- [80] M. de Jong, W. Chen, T. Angsten, A. Jain, R. Notestine, A. Gamst, M. Sluiter, C. Krishna Ande, S. van der Zwaag, J. J. Plata, C. Toher, S. Curtarolo, G. Ceder, K. A. Persson, and M. Asta, “Charting the complete elastic properties of inorganic crystalline compounds,” *Scientific Data*, vol. 2, Mar. 2015.
- [81] A. Reuß, “Berechnung der fließgrenze von mischkristallen auf grund der plastizitätsbedingung für einkristalle.,” *ZAMM-Journal of Applied Mathematics and Mechanics/Zeitschrift für Angewandte Mathematik und Mechanik*, vol. 9, no. 1, pp. 49–58, 1929.
- [82] W. Voigt, *Lehrbuch der Kristallphysik*. Vieweg+Teubner Verlag, 1966.
- [83] K. Nishimura, R. K. Kalia, A. Nakano, and P. Vashishta, “Nanoindentation hardness anisotropy of alumina crystal: A molecular dynamics study,” *Applied Physics Letters*, vol. 92, Apr. 2008.
- [84] A. D. S. Jayatilaka and K. Trustrum, “Statistical approach to brittle fracture,” *Journal of Materials Science*, vol. 12, p. 1426–1430, July 1977.
- [85] A. A. Griffith, “VI. the phenomena of rupture and flow in solids,” *Philosophical Transactions of the Royal Society of London. Series A, Containing Papers of a Mathematical or Physical Character*, vol. 221, p. 163–198, Jan. 1921.
- [86] S. Bavdekar and G. Subhash, *Failure Mechanisms of Ceramics Under Quasi-static and Dynamic Loads: Overview*, p. 579–607. Springer International Publishing, 2022.
- [87] T. Antoun, D. Curran, S. V. Razorenov, L. Seaman, G. I. Kanel, and A. V. Utkin, *Spallation in Materials of Different Classes*, pp. 137–173. New York, NY: Springer New York, 2003.
- [88] J. Zheng, H. Li, and J. Hogan, “Strain-rate-dependent tensile response of an alumina ceramic: Experiments and modeling,” *International Journal of Impact Engineering*, vol. 173, p. 104487, Mar. 2023.

- [89] F. Galvez, J. Rodriguez, and V. Sanchez Galvez, “Influence of the strain rate on the tensile strength in aluminas of different purity,” *Le Journal de Physique IV*, vol. 10, pp. Pr9–323–Pr9–328, Sept. 2000.
- [90] F. Galvez Diaz-Rubio, J. Rodriguez Perez, and V. Sanchez Galvez, “The spalling of long bars as a reliable method of measuring the dynamic tensile strength of ceramics,” *International Journal of Impact Engineering*, vol. 27, p. 161–177, Feb. 2002.
- [91] A. Stukowski, V. Bulatov, and A. Arsenlis, “Automated identification and indexing of dislocations in crystal interfaces,” *Modelling and Simulation in Materials Science and Engineering*, vol. 20, no. 8, p. 085007, 2012.
- [92] Z. Chen, X. Zhang, W. Li, and X. Yao, “Shock compression of nanoporous silicon carbide at high strain rate,” *International Journal of Mechanical Sciences*, vol. 224, p. 107320, June 2022.

Supplemental Material

Spall failure of alumina at high-strain rates using femtosecond laser experiments and high-fidelity molecular dynamics simulations

Mewael Isiet, Musanna Galib, Yunhuan Xiao, Jerry I. Dadap, Ziliang Ye, Mauricio Ponga

Postmortem surface micrographs of interface failure

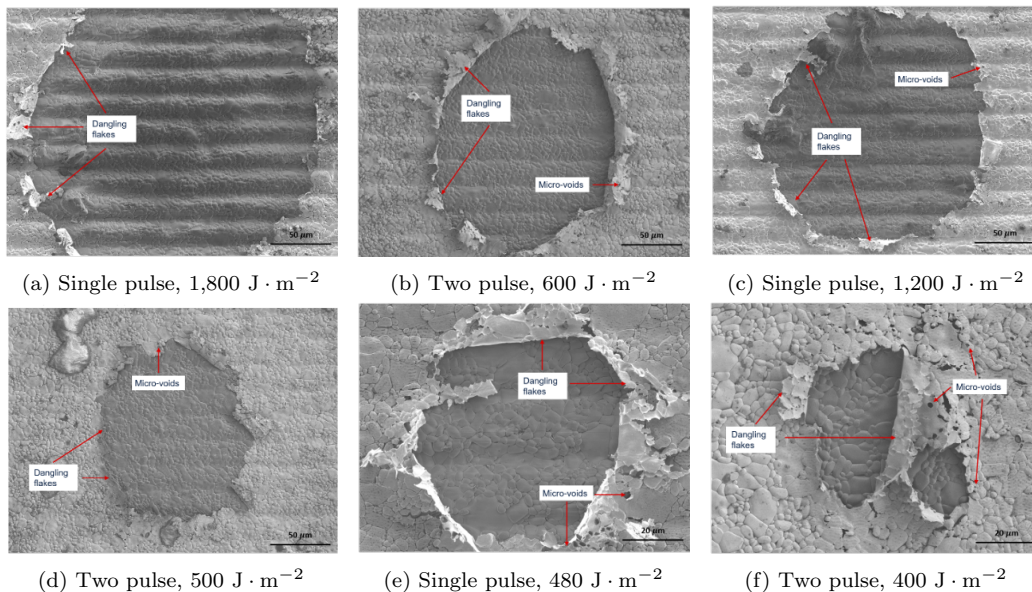


Figure S1: Closeup SEM images of the (front) surface features produced after single- and two-pulse laser illumination on the nickel coated Al_2O_3 for a range of laser fluence between $1,800$ to $400 \text{ J} \cdot \text{m}^{-2}$. In these images, the Ni coating (visible as silver toned) is displayed with the underlying Al_2O_3 substrate exposed with varying degrees depending on the laser fluence. Furthermore, dangling Ni flakes and micro-voids on the Ni coating can be seen under both approaches.

Pore distribution in post laser-shocked alumina

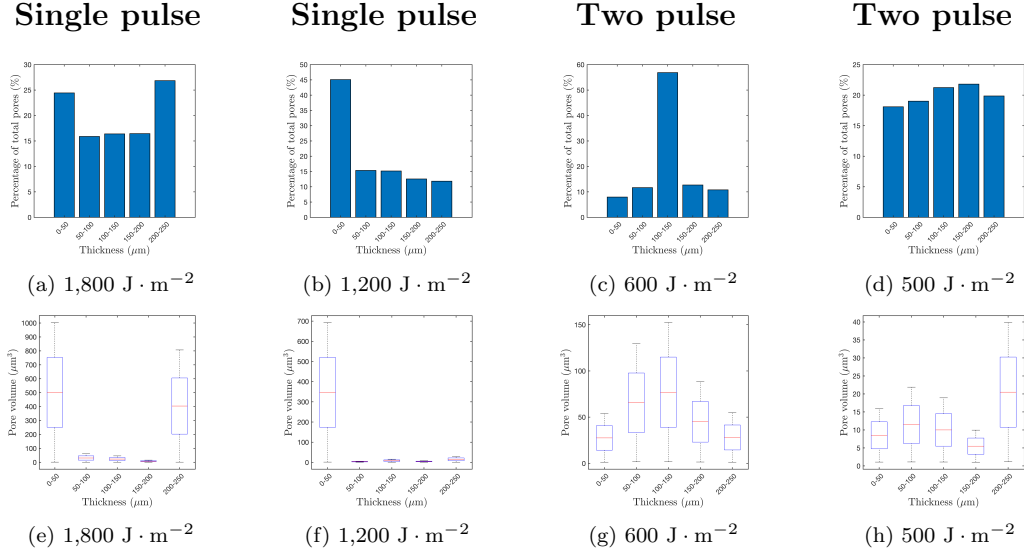


Figure S2: Porosity analysis of the Al_2O_3 sample illuminated by the single- and two-pulse laser approaches with (a–d) highlighting the distribution of pore count percentage as a function of thickness and (e–h) illustrating the boxplot of pore volume distribution across thickness, highlighting statistical variations. These results provide insight into the two-pulse approach ability to nucleate voids at the centre of the sample similar to the plate-impact method.

The effect of the single- (fluence: $1,800$ and $1,200 \text{ J} \cdot \text{m}^{-2}$) and two-pulse approach (fluence: 600 and $500 \text{ J} \cdot \text{m}^{-2}$) on the pore (void) distribution in Al_2O_3 can be seen in Figure S2. To investigate the pore distribution across thickness, multiple 50 nm -wide slices of the 3D reconstructed sample were created along the laser-pulse direction. In the single-pulse approach at $1,800 \text{ J} \cdot \text{m}^{-2}$, failure primarily occurred near the front and back surfaces (i.e., the $0\text{-}50$ and $200\text{-}250 \text{ nm}$ bins) due to the passage of the unloading tensile wave and the interaction of the reflected compressive wave with the unloading wave near the back surface (see Figures S2a–S2e and 3b). At $1,200 \text{ J} \cdot \text{m}^{-2}$, failure was observed only near the front surface—closer to the illuminated surface—indicating that classical spall failure (under the single-pulse approach), which typically results from the interaction of the reflected compressive wave with the unloading wave near the back surface, did not occur in this case. As for the two-pulse approach under $600 \text{ J} \cdot \text{m}^{-2}$, the interaction of the unloading tensile waves at the sample center generated large hydrostatic stress, leading

to failure predominantly taking place at the center (corresponding to the 100-150 nm bin) as shown in Figure S2c. Additionally, bins closer to the center (50–100 nm and 150–200 nm) exhibited a higher void density than those near the surface. Furthermore, the median, largest pore volume, and interquartile range of the pore distribution followed a similar trend, as shown in Figure S2g. At $500 \text{ J} \cdot \text{m}^{-2}$, despite an increase in the median and largest pore volume at the back surface (200–250 nm) compared to other regions, minimal spall features were observed when comparing the porosity analysis with the pristine sample (see Figures 1b and 3e). Hence, this analysis highlights (a) the laser fluence threshold for spallation in the single- and two-pulse laser approaches, identified as $1,800$ and $600 \text{ J} \cdot \text{m}^{-2}$, respectively and (b) the ability of the two-pulse approach to produce central voids, which correlates to the observed failure patterns seen in the 2D micro-CT slices, as shown in Figure 3.

Interatomic potential stress-strain prediction for alumina

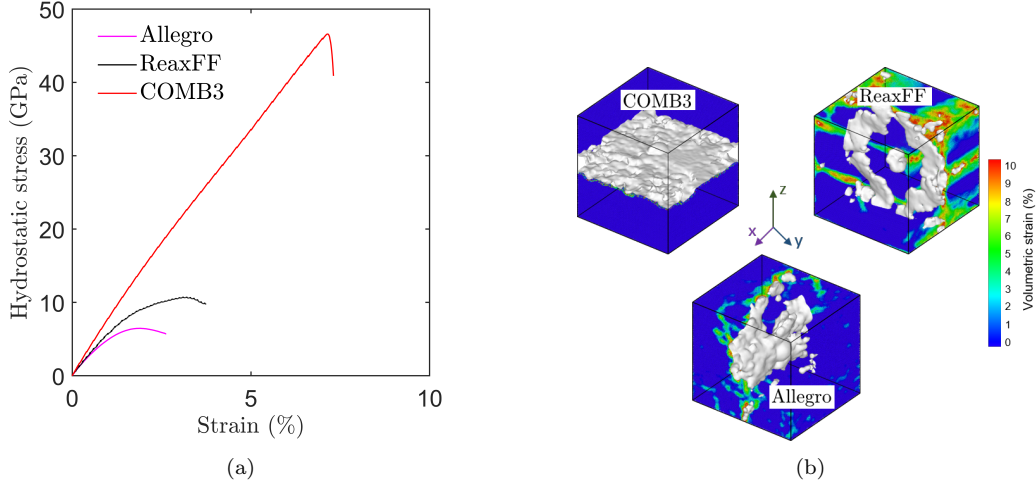


Figure S3: Application of reactive, COMB3 and ReaxFF, and machine learning, Allegro, force fields to predict the (a) stress-strain behaviour and (b) failure pattern, at a strain of 5%, of Al_2O_3 under a strain rate of 10^9 s^{-1} for a simulation cell with a volume of 30 nm^3 and a nano-void diameter of 6 nm. A surface mesh, based on the alpha-shape method [S91], is imposed on the simulation cell to highlighted the failure pattern predicted under the molecular dynamics simulations.

Figure S3a highlights the stress-strain curve calculated using three different interatomic potentials. It can be seen that the Allegro potential predicted a much lower peak stress, i.e., spall strength, in comparison to the other potentials. In comparison, the spall strength (and critical strain) predicted by Allegro is 6.5 GPa (1.9%), whereas ReaxFF and COMB3 are 10.8 (3.2%) and 46.8 GPa (7.1%), respectively. It can be seen that all potentials predicted an initial linear trend, however it can be seen that slope of the stress-strain curves differ. On the one hand, the COMB potential predicts an almost constant slope, whereas the Allegro and ReaxFF predicted a reduction in the slope with increasing strain - this difference can be attributed to the elastic constant tensor dependence on deformation.

The predicted failure pattern by the three force fields is given in Figure S3b. The COMB potential predicted a single failure plane along the XY plane, however, the Allegro and ReaxFF potentials predicted failure along the XZ and YZ plane, respectively. Also, the COMB and Allegro potentials correctly predicted failure at the vicinity of the nanovoid, where as the

ReaxFF potential predicted failure away from the nanovoid. Lastly, bond breakage, prior to microcrack formation and propagation, was predicted by the Allegro and ReaxFF potentials, however, the COMB potential predicted nearly instantaneous failure once the critical strain was achieved. Overall, the Allegro potential managed to predict a lower spall strength and critical strain, while predicting a brittle failure involving bond breakage, microcrack formation, and crack propagation and showing good agreement with DFT calculated elastic constants in Table 1. Hence, this makes the Allegro potential a good alternative to the other classical reactive force fields, i.e., ReaxFF and COMB.

Bond breakage mechanism in alumina

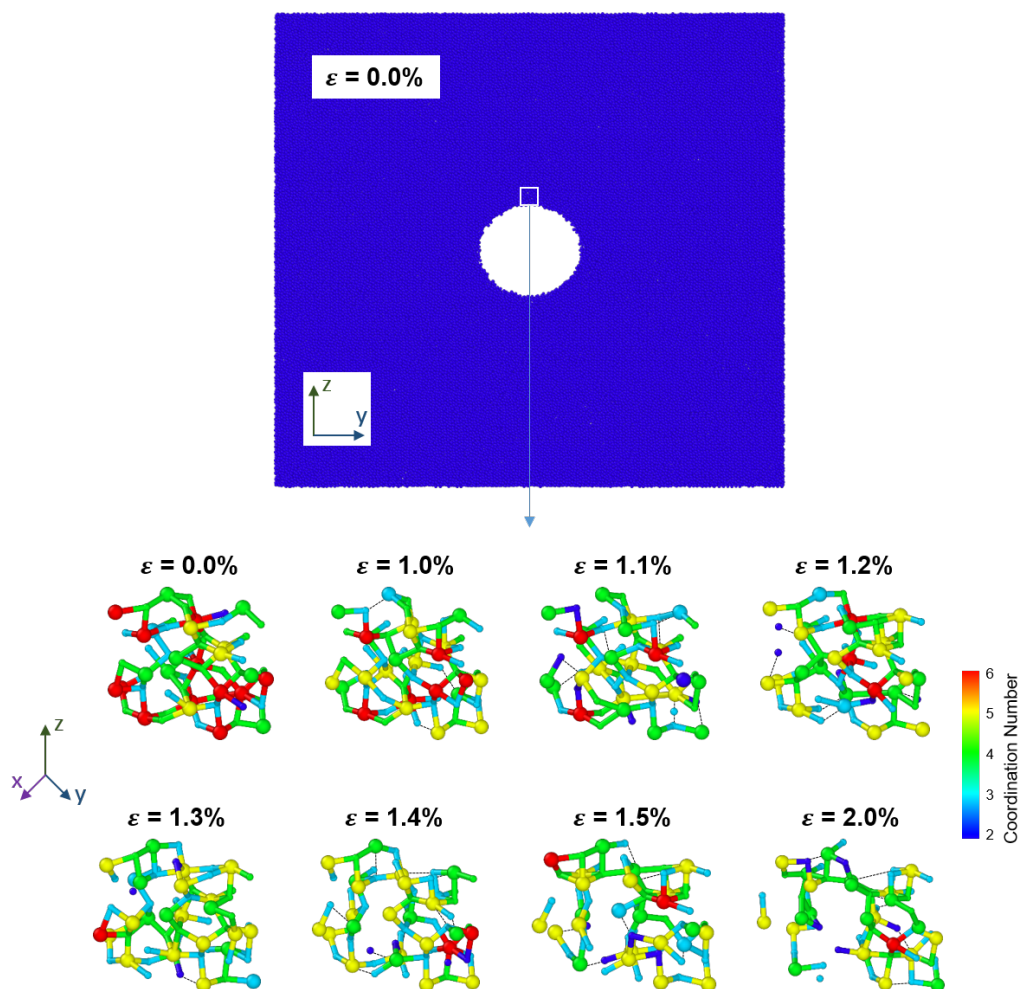


Figure S4: Bond breakage in Al_2O_3 predicted under hydro-static loading with a strain rate of 10^8 s^{-1} for a simulation cell with a volume of 30 nm^3 and a nano-void diameter of 6 nm . Here the black dashed line corresponds to a broken bond.

Failure behavior of alumina along XY and XZ plane

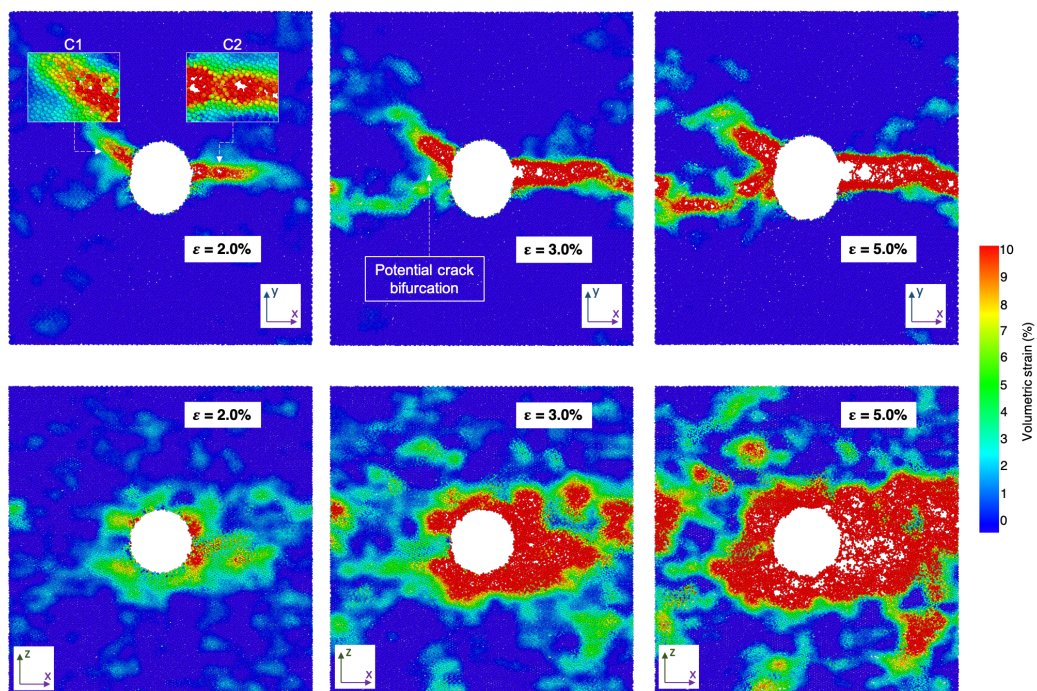


Figure S5: Molecular dynamics simulation of Al_2O_3 under hydrostatic loading highlighting the spall behaviour along the **XY** and **XZ** plane under a strain rate of 10^8 s^{-1} for a simulation cell with a volume of 30 nm^3 and a nano-void diameter of 6 nm .

Evolution of failure in alumina with increasing strain

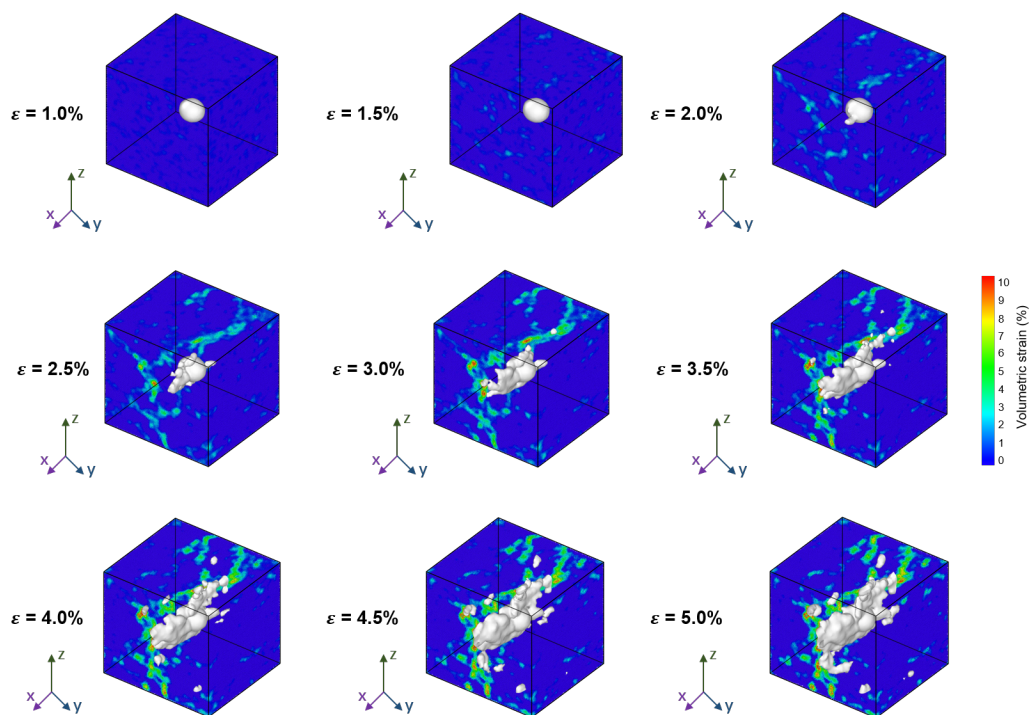


Figure S6: Schematic of the brittle failure of Al_2O_3 under hydrostatic loading with a strain rate of 10^8 s^{-1} from 1.0 % to 5.0 % with a 6 nm diameter void. A surface mesh, based on the alpha-shape method [S91], is imposed on the simulation cell to highlighted the failure pattern predicted under the molecular dynamics simulations.

Nanovoid size effect on spall behavior of alumina

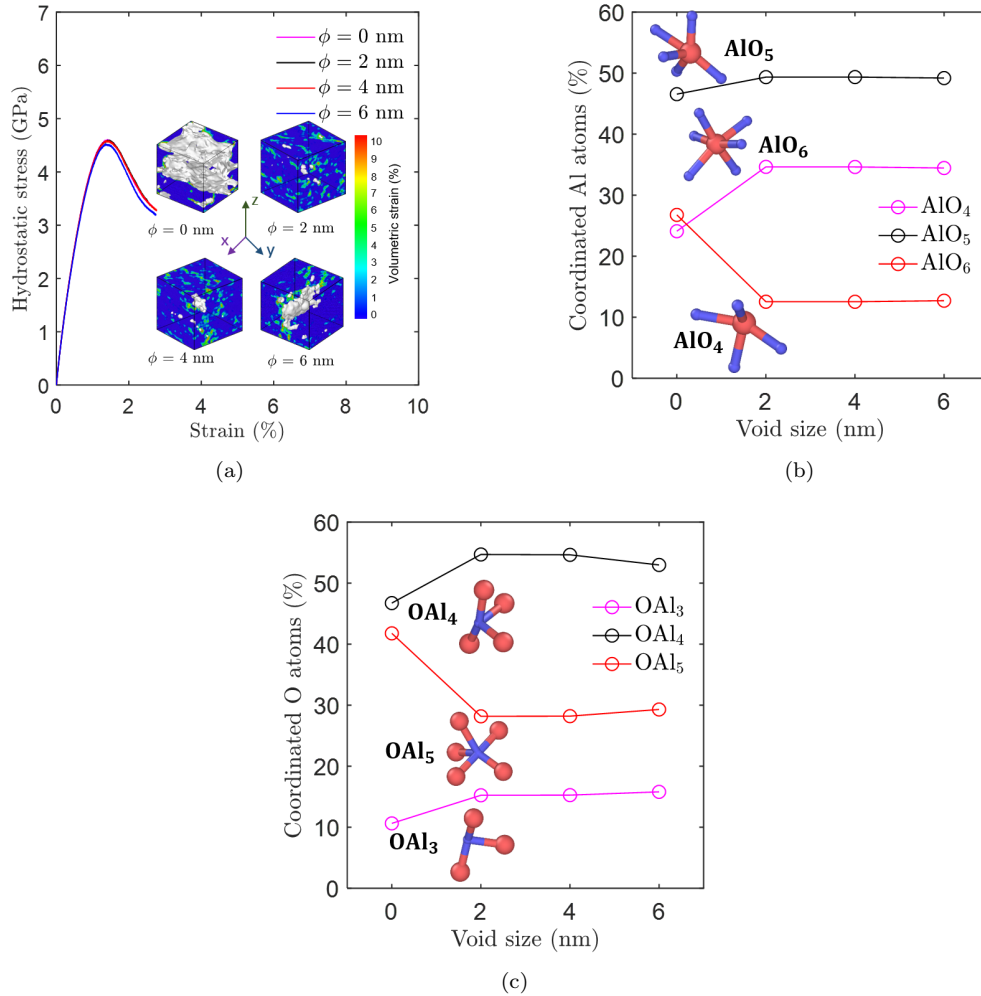


Figure S7: Effect of nanovoid size on Al_2O_3 (a) stress-strain behavior with inset figures of the predicted failure pattern for the selected nanovoid size simulation, and coordination number of (b) Al and (c) O atoms at strain of 5%. Simulations were conducted with a strain rate of 10^8 s^{-1} for a simulation cell with a volume of 30 nm^3 .

The effect of void size on the stress-strain behaviour is depicted in Figure S7a. In these simulations, the void diameter was varied between 0 and 6 nm. Notably, the spall strength for the defect-free Al_2O_3 is $\sigma_{\text{spall}} = 4.6$ GPa. In contrast, the introduction of nanosized voids led to a reduction in

spall strength from 4.6 to 4.45 GPa, although the critical strain remained constant at 1.4%. Interestingly, a distinct transition is observed when comparing the defect-free case to samples with nanovoids. Failure analysis reveals a decrease in the extent of failure as void size increases, as shown in the inset images of Figure S7a. This was observed by tracking the void volume, which was visualized using surface meshes. Defect-free samples exhibited brittle failure along multiple spall planes due to lack of any weak spots or stress concentration sites. Conversely, samples containing nanovoids failed predominantly along a single spall plane, with increasing damage correlated to larger void diameters. Additionally, coordination analysis indicated a rise in bond breakage, evident by the decrease in AlO_6 and OAl_5 and increase in the other coordinated Al and O atoms, with increasing void size for both Al and O atoms as seen in Figures S7b—S7c. Comparatively, nanovoid cases exhibited significantly more bond breakage than the defect-free samples. This transition in failure behavior arises directly from the increased void size, a phenomenon well established in the literature. It is known that an increase in initial defect size reduces the stress-carrying capacity of materials, a trend consistent with our findings and previous studies [S92, S42].